Journal of Sound and Vibration 523 (2022) 116692

Contents lists available at ScienceDirect

Journal of Sound and Vibration

journal homepage: www.elsevier.com/locate/jsvi

Retrospective cost adaptive harmonic disturbance rejection using dereverberated target models

Nima Mohseni *, Dennis S. Bernstein

Department of Aerospace Engineering, University of Michigan, 1320 Beal Ave., Ann Arbor MI 48109, United States of America

ARTICLE INFO

Keywords:
Adaptive control
Vibration suppression
Dereverberated transfer function
Sampled-data control

ABSTRACT

This paper focuses on adaptive feedback disturbance rejection for lightly damped structures using retrospective cost adaptive control (RCAC). RCAC uses a target model of the closed-loop dynamics in order to enable controller adaptation. The target model captures specific features of the dynamics of the structure; in the SISO case, this information consists of the sign of the leading numerator coefficient, relative degree, and nonminimum-phase zeros of the discretized dynamics. The present paper investigates the feasibility of using a dereverberated transfer function (DTF) as the target model for harmonic disturbance rejection with unknown disturbances. In particular, the dereverberated target model (DTM) obtained by magnitude and phase averaging captures the magnitude and phase trend of the structure but ignores resonances and anti-resonances, thus providing a low-order target model for controller adaptation. The robustness of RCAC is investigated with the target model given by a DTF based on a nominal model with erroneous damping ratio. The technique is implemented experimentally on an acoustic noise control setup.

1. Introduction

Feedback disturbance rejection for high-order, lightly damped structures and acoustic spaces is a longstanding challenge in control theory and technology [1–3]. Applications of this technology range from space apertures (optical and RF) to positioning mechanisms in hard drives [4,5]. The difficulty of the problem stems from the high dimensionality—theoretically infinite—of the structural dynamics, the proximity of the poles to the imaginary axis, the presence of nonminimum-phase zeros, and model uncertainty due to limitations in analytical and empirical modeling. Additional challenges arise from loop coupling in MIMO applications, time delays due to wave propagation, limitations in sensors, actuators, and computation, and spectral and spatial spillover.

A widely studied approach to controlling lightly damped structures is to assume that the sensors and actuators are chosen and placed such that the plant transfer function is positive real [6–8]. Under this assumption, the weights for LQG controller synthesis can be chosen such that the LQG control is positive real, thus guaranteeing closed-loop stability [9]. In practice, however, positivity assumptions are often violated [10]. Consequently, feedback control of lightly damped structures remains challenging and relevant to diverse applications.

Although feedback control can modify the dynamics of a structure, for example, by adding damping or altering mode shapes, this approach has inherent limitations [11] and can destabilize the structure. In view of these challenges, a popular approach is adaptive feedforward disturbance rejection, which uses either a measurement of the disturbance or a closely related sensor signal, such as

* Corresponding author.
E-mail address: nmohseni@umich.edu (N. Mohseni).

https://doi.org/10.1016/j.jsv.2021.116692
Received 19 December 2020; Received in revised form 24 October 2021; Accepted 10 December 2021
Available online 4 January 2022

an engine tachometer. One of the most successful feedforward control algorithms for adaptive disturbance rejection is filtered-x least-mean-square (FxLMS) [3,12,13], which uses knowledge of the secondary-path (control-to-error-signal) dynamics to update the coefficients of a finite-impulse-response (FIR) controller.

In some applications, however, a measurement of the disturbance is not available. This situation arises, for example, when the disturbance enters the structure in a spatially distributed manner, such as in the case of broadband road and wind noise. Another impediment occurs when the control signal used to cancel the disturbance corrupts the disturbance sensor, as in the case of speakers and microphones inside a vehicle. In these and other situations where feedforward disturbance rejection is not applicable, feedback control is of interest. Fixed-gain, feedback control methods, including optimal and robust techniques, have been widely studied [14]. Uncertainty in the high-order, lightly damped dynamics, however, motivates the need for adaptive feedback control techniques.

The present paper focuses on retrospective cost adaptive control (RCAC) for lightly damped structures with uncertain dynamics and disturbance spectrum [15]. The modeling information required by RCAC resides in the *target model* of the closed-loop dynamics; as shown in [15], construction of this model depends on key features of the dynamics of the structure. In the SISO case, this information includes knowledge of the sign of the leading numerator coefficient, relative degree, and nonminimum-phase zeros of the discretized dynamics. In the MIMO case, the required information is obtained through a collection of impulse-response matrices [16]. Stability analysis of RCAC is given in [17] for minimum-phase systems and in [18] for nonminimum-phase systems.

The goal of the present paper is to investigate the feasibility of using a *dereverberated transfer function (DTF)* as the target model. A dereverberated model of a lightly damped structure captures the magnitude and phase trend but ignores resonances and anti-resonances [19–22]. A DTF is thus an approximate, low-order model of a lightly damped structure that can easily be obtained in practice and is insensitive to details of lightly damped poles and zeros. The present paper investigates the performance and robustness of RCAC when the target model is chosen to be a DTF based on a nominal model of the structure. The use of a DTF in adaptive feedback disturbance rejection is a novel feature of the present paper.

Various techniques have been developed for generating a DTF from an analytical or empirical model of a structure [23–26]. All of these techniques capture some aspect of the mean of the frequency response, for example, by optimizing the logarithmic-average of the magnitude of the frequency response. Along these lines, the present paper extends the method used in [19] by accounting for both the magnitude and phase of the frequency response.

The present paper investigates the performance and robustness of RCAC when a DTF is used as the target model. Since the DTF ignores details of the frequency response, the goal is to investigate the effect of the magnitude and phase difference between the target model and the open-loop transfer function at the frequency of the harmonic disturbance. This difference can be viewed as modeling error; however, the target model is not intended to be a high-fidelity model of the open-loop structure, but rather a rudimentary model of the desired closed-loop dynamics. Therefore, at each disturbance frequency, we compare the magnitude and phase difference between the target model and the open-loop transfer function to the magnitude and phase difference between the target model and the closed-loop transfer function. The case where the latter magnitude and phase difference is smaller in absolute value than the former indicates that the adaptation has correctly matched the closed-loop dynamics to the target model at the disturbance frequency. The ability of RCAC to perform this matching for both nominal and off-nominal dynamics provides a measure of the robustness of RCAC to variations in the physical structure.

In practice, accurate estimates of the modal damping are often unavailable, and thus the target model may be created from a model with erroneous damping ratios. Section 5 investigates the robustness of the adaptive controller to errors in damping. The DTF is created using a nominal model, and the adaptive controller is applied to a structure with different values of the damping ratio. To assess robustness, the asymptotic closed-loop response is compared to the open-loop response level over a range of off-nominal damping ratios.

The paper is structured as follows. Section 2 describes the disturbance rejection problem, the RCAC algorithm, and the standard construction of the target model. A method for generating a DTF is presented in Section 3. Sections 4, and 5 investigate harmonic disturbance rejection using RCAC with a DTF as the target model. Finally, adaptive control of a MISO acoustic experiment using a MISO dereverberated target model is described in Section 6.

2. Retrospective cost adaptive control

2.1. Sampled-data disturbance rejection problem

The disturbance rejection problem involves four signals, namely, the performance z, the disturbance w, the output y, and the control u. These signals are related by the transfer functions G_{zu}, G_{zw}, G_{yu}, and G_{yw}, which define the continuous-time, input–output model

$$z(t) = G_{zw}(\mathbf{p})w(t) + G_{zu}(\mathbf{p})u(t), \tag{1}$$

$$y(t) = G_{yw}(\mathbf{p})w(t) + G_{yu}(\mathbf{p})u(t), \tag{2}$$

where $\mathbf{p}$ is the differentiation operator $\mathrm{d}/\mathrm{d}t$. The signals $y(t)$ and $z(t)$ are sampled instantaneously to obtain $y_k \triangleq y(kT_s) \in \mathbb{R}^{l_y}$ and $z_k \triangleq z(kT_s) \in \mathbb{R}^{l_z}$, and the control $u(t) \equiv u_k \in \mathbb{R}^{l_u}$ for all $t \in [kT_s, (k+1)T_s)$ is reconstructed from u_k using a zero-order hold (ZOH). The feedback controller $G_c(\mathbf{q}, \hat{\theta})$, where $\mathbf{q}$ is the forward-shift operator and $\hat{\theta}$ is a vector of controller coefficients that is updated at each step, uses y_k to determine u_k, as shown in Fig. 1. In order to suppress the effect of the disturbance $w(t)$ on z_k, the adaptive controller uses measurements of z_k to update $G_c(\mathbf{q}, \hat{\theta})$. The controller update is indicated by the diagonal line in Fig. 1,

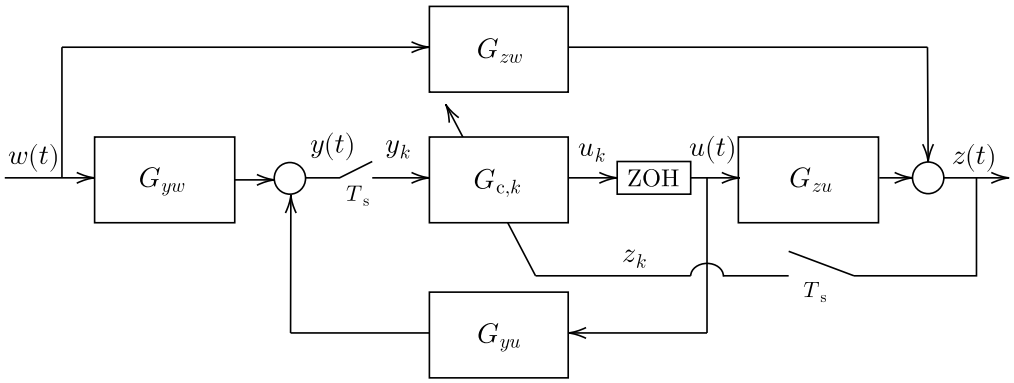

Fig. 1. Block diagram of the sampled-data adaptive disturbance rejection architecture. The controller $G_{c,k}$ is updated at each time step k.

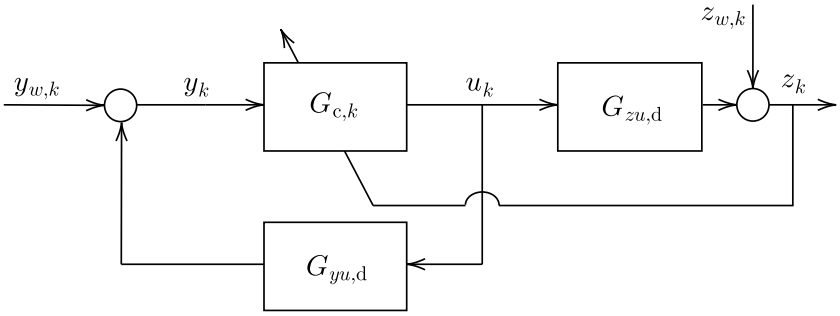

Fig. 2. Block diagram of the sampled-data adaptive disturbance rejection architecture in discrete time.

It follows from Eqs. (1) and (2) that z_k and y_k are given by

$$z_k = z_{w,k} + G_{zu,\mathrm{d}}(\mathbf{q})u_k, \tag{3}$$

$$y_k = y_{w,k} + G_{yu,\mathrm{d}}(\mathbf{q})u_k, \tag{4}$$

where

$$z_{w,k} \triangleq C_{zw}\int_{(k-1)T_s}^{kT_s} e^{A_{zw}(kT_s-t)}B_{zw}w(t)\,\mathrm{d}t + D_{zw}\int_{(k-1)T_s}^{kT_s} w(t)\,\mathrm{d}t, \tag{5}$$

$$y_{w,k} \triangleq C_{yw}\int_{(k-1)T_s}^{kT_s} e^{A_{yw}(kT_s-t)}B_{yw}w(t)\,\mathrm{d}t + D_{yw}\int_{(k-1)T_s}^{kT_s} w(t)\,\mathrm{d}t, \tag{6}$$

where $(A_{zw}, B_{zw}, C_{zw}, D_{zw})$ and $(A_{yw}, B_{yw}, C_{yw}, D_{yw})$ are realizations of $G_{zu}(\mathbf{p})$ and $G_{yu}(\mathbf{p})$, respectively, and $G_{zu,\mathrm{d}}(\mathbf{q})$ and $G_{yu,\mathrm{d}}(\mathbf{q})$ are the zero-order hold discretizations of $G_{zu}(\mathbf{p})$ and $G_{yu}(\mathbf{p})$, respectively. A block diagram of the discrete-time disturbance rejection problem is shown in Fig. 2. All simulation based examples in the paper are conducted in a sample-data feedback loop with integration between samples using *ode45* in order to capture the intersample behavior.

2.2. RCAC algorithm

For the current vector θ_k of controller coefficients, $G_c(\mathbf{q}, \theta_k)$ is realized by the linear, time-varying, input–output model

$$u_k = \sum_{i=1}^{n_c} P_{i,k}u_{k-i} + \sum_{i=1}^{n_c} Q_{i,k}y_{k-i} \tag{7}$$

where $P_{i,k} \in \mathbb{R}^{l_u \times l_u}$, $Q_{i,k} \in \mathbb{R}^{l_u \times l_y}$, and n_c is the controller order. The startup protocol for Eq. (7) is given by

$$u_k = \begin{cases} 0, & k < k_w, \\ \Phi_k\theta_k, & k \geq k_w, \end{cases} \tag{8}$$

where the regressor matrix Φ_k is defined as

$$\Phi_k \triangleq \begin{bmatrix} u_{k-1} \\ \vdots \\ u_{k-n_c} \\ y_{k-1} \\ \vdots \\ y_{k-n_c} \end{bmatrix}^{\mathrm{T}} \otimes I_{l_u} \in \mathbb{R}^{l_u \times l_\theta}, \tag{9}$$

$k_w \geq n_c$ is the number of steps to wait until Φ_k is populated with data, θ_k is the controller coefficient vector defined by

$$\theta_k \triangleq \operatorname{vec} \begin{bmatrix} P_{1,k} & \cdots & P_{n_c,k} & Q_{1,k} & \cdots & Q_{n_c,k} \end{bmatrix}^{\mathrm{T}} \in \mathbb{R}^{l_\theta}, \tag{10}$$

and $l_\theta \triangleq n_c l_u (l_u + l_y)$.

The retrospective performance variable is defined by

$$\hat{z}_k(\hat{\theta}) \triangleq z_k - G_{\mathrm{f}}(\mathbf{q})(u_k - \Phi_k \hat{\theta}), \tag{11}$$

where $\hat{\theta}$ is the controller coefficient vector to be optimized, and $G_{\mathrm{f}}(\mathbf{q}) \in \mathbb{R}^{l_z \times l_u}$ is a filter. As discussed in Section 2.4, G_{f} plays the role of the target model for a closed-loop transfer function. Defining the filtered quantities $u_{\mathrm{f},k} \triangleq G_{\mathrm{f}}(\mathbf{q})u_k$ and $\Phi_{\mathrm{f},k} \triangleq G_{\mathrm{f}}(\mathbf{q})\Phi_k$, Eq. (11) can be written as

$$\hat{z}_k(\hat{\theta}) = z_k - (u_{\mathrm{f},k} - \Phi_{\mathrm{f},k}\hat{\theta}). \tag{12}$$

The controller coefficient vector $\hat{\theta}$ is updated by minimizing the cost function

$$J_k(\hat{\theta}) \triangleq \sum_{i=1}^{k} \lambda^{k-i} [\hat{z}_i(\hat{\theta})^{\mathrm{T}} R_z \hat{z}_i(\hat{\theta}) + (\Phi_i \hat{\theta})^{\mathrm{T}} R_u (\Phi_i \hat{\theta})] + \lambda^k (\hat{\theta} - \theta_0)^{\mathrm{T}} R_\theta (\hat{\theta} - \theta_0) \tag{13}$$

where $\lambda \in (0, 1]$ is the forgetting factor, $R_\theta \in \mathbb{R}^{l_\theta \times l_\theta}$ and $R_z \in \mathbb{R}^{l_z \times l_z}$ are positive definite, and $R_u \in \mathbb{R}^{l_u \times l_u}$ is positive semidefinite. Using recursive least squares (RLS), the update law for the controller coefficient vector is given by

$$\theta_{k+1} = \theta_k - P_k \begin{bmatrix} \Phi_{\mathrm{f},k} \\ \Phi_k \end{bmatrix}^{\mathrm{T}} \left(\lambda \begin{bmatrix} R_z & 0 \\ 0 & R_u \end{bmatrix}^{-1} + \begin{bmatrix} \Phi_{\mathrm{f},k} \\ \Phi_k \end{bmatrix} P_k \begin{bmatrix} \Phi_{\mathrm{f},k} \\ \Phi_k \end{bmatrix}^{\mathrm{T}} \right)^{-1} \left(\begin{bmatrix} \Phi_{\mathrm{f},k} \\ \Phi_k \end{bmatrix} \theta_k + \begin{bmatrix} z_k - u_{\mathrm{f},k} \\ 0 \end{bmatrix} \right) \tag{14}$$

where

$$P_{k+1} = \frac{1}{\lambda} P_k - \frac{1}{\lambda} P_k \begin{bmatrix} \Phi_{\mathrm{f},k} \\ \Phi_k \end{bmatrix}^{\mathrm{T}} \left(\lambda \begin{bmatrix} R_z & 0 \\ 0 & R_u \end{bmatrix}^{-1} + \begin{bmatrix} \Phi_{\mathrm{f},k} \\ \Phi_k \end{bmatrix} P_k \begin{bmatrix} \Phi_{\mathrm{f},k} \\ \Phi_k \end{bmatrix}^{\mathrm{T}} \right)^{-1} \begin{bmatrix} \Phi_{\mathrm{f},k} \\ \Phi_k \end{bmatrix} P_k \tag{15}$$

and $P_0 = R_\theta^{-1}$ [27]. The RLS update law has a computational complexity of $O(l_\theta^2)$.

2.3. Analysis of the closed-loop dynamics

Defining

$$\bar{u}_k(\hat{\theta}) \triangleq \Phi_k \hat{\theta}, \tag{16}$$

$$\tilde{u}_k(\hat{\theta}) \triangleq u_k - \bar{u}_k(\hat{\theta}) = u_k - \Phi_k \hat{\theta}, \tag{17}$$

Eq. (11) can be written as

$$\hat{z}_k(\hat{\theta}) = z_k - G_{\mathrm{f}}(\mathbf{q})\tilde{u}_k(\hat{\theta}). \tag{18}$$

Next, using Eqs. (7) and (17), the controller $G_{\mathrm{c}}(\mathbf{q}, \hat{\theta})$ corresponding to $\hat{\theta}$ is realized as

$$\bar{u}_k(\hat{\theta}) = \sum_{i=1}^{n_c} \hat{P}_i u_{k-i} + \sum_{i=1}^{n_c} \hat{Q}_i y_{k-i} \tag{19}$$

$$= \sum_{i=1}^{n_c} \hat{P}_i \bar{u}_{k-i}(\hat{\theta}) + \sum_{i=1}^{n_c} \hat{P}_i \tilde{u}_{k-i}(\hat{\theta}) + \sum_{i=1}^{n_c} \hat{Q}_i y_{k-i}, \tag{20}$$

which implies that

$$\bar{u}_k(\hat{\theta}) = D_{\mathrm{c}}^{-1}(\mathbf{q}, \hat{\theta})[(\mathbf{q}^{n_c} I_{l_u} - D_{\mathrm{c}}(\mathbf{q}, \hat{\theta}))\tilde{u}_k(\hat{\theta}) + N_{\mathrm{c}}(\mathbf{q}, \hat{\theta}) y_k], \tag{21}$$

where

$$N_{\mathrm{c}}(\mathbf{q}, \hat{\theta}) \triangleq \mathbf{q}^{n_c - 1}\hat{Q}_1 + \cdots + \hat{Q}_{n_c}, \tag{22}$$

$$D_{\mathrm{c}}(\mathbf{q}, \hat{\theta}) \triangleq \mathbf{q}^{n_c} I_{l_u} - \mathbf{q}^{n_c - 1}\hat{P}_1 - \cdots - \hat{P}_{n_c}. \tag{23}$$

Next, defining

$$G_{\mathrm{c}}(\mathbf{q},\hat{\theta}) \triangleq D_{\mathrm{c}}^{-1}(\mathbf{q},\hat{\theta})N_{\mathrm{c}}(\mathbf{q},\hat{\theta}) \tag{24}$$

and substituting Eqs. (17) and (21) into Eqs. (3) and (4) yields

$$z_k = z_{w,k} + G_{zu,\mathrm{d}}(\mathbf{q})\left(D_{\mathrm{c}}^{-1}(\mathbf{q},\hat{\theta})[(\mathbf{q}^{n_{\mathrm{c}}}I_{l_u} - D_{\mathrm{c}}(\mathbf{q},\hat{\theta}))\tilde{u}_k(\hat{\theta}) + N_{\mathrm{c}}(\mathbf{q},\hat{\theta})y_k] + \tilde{u}_k(\hat{\theta})\right), \tag{25}$$

$$y_k = y_{w,k} + G_{yu,\mathrm{d}}(\mathbf{q})\left(D_{\mathrm{c}}^{-1}(\mathbf{q},\hat{\theta})[(\mathbf{q}^{n_{\mathrm{c}}}I_{l_u} - D_{\mathrm{c}}(\mathbf{q},\hat{\theta}))\tilde{u}_k(\hat{\theta}) + N_{\mathrm{c}}(\mathbf{q},\hat{\theta})y_k] + \tilde{u}_k(\hat{\theta})\right), \tag{26}$$

where $z_{w,k}$ and $y_{w,k}$ are defined by Eqs. (5) and (6). Finally, solving Eq. (26) for y_k and substituting y_k into Eq. (25) yields

$$z_k = \xi_k(\hat{\theta}) + \tilde{G}_{z\tilde{u}}(\mathbf{q},\hat{\theta})\tilde{u}_k(\hat{\theta}), \tag{27}$$

where

$$\xi_k(\hat{\theta}) \triangleq z_{w,k} + G_{zu,\mathrm{d}}(\mathbf{q})G_{\mathrm{c}}(\mathbf{q},\hat{\theta})(I_{l_y} - G_{yu,\mathrm{d}}(\mathbf{q})G_{\mathrm{c}}(\mathbf{q},\hat{\theta}))^{-1}y_{w,k}, \tag{28}$$

$$\tilde{G}_{z\tilde{u}}(\mathbf{q},\hat{\theta}) \triangleq \mathbf{q}^{n_{\mathrm{c}}}G_{zu,\mathrm{d}}(\mathbf{q})\left(D_{\mathrm{c}}^{-1}(\mathbf{q},\hat{\theta}) + G_{\mathrm{c}}(\mathbf{q},\hat{\theta})[I_{l_y} - G_{yu,\mathrm{d}}(\mathbf{q})G_{\mathrm{c}}(\mathbf{q},\hat{\theta})]^{-1}G_{yu,\mathrm{d}}(\mathbf{q})D_{\mathrm{c}}^{-1}(\mathbf{q},\hat{\theta})\right). \tag{29}$$

Note that $\xi_k(\hat{\theta})$ is the portion of the measurement z_k due to $w(t)$ when using the controller $G_{\mathrm{c}}(\mathbf{q},\hat{\theta})$. Finally, note that Eqs. (16)–(29) are valid for all $\hat{\theta} \in \mathbb{R}^{l_\theta}$.

2.4. Optimal controller and the target model

Now, assume that there exists θ^* that minimizes Eq. (13) for all k, and define

$$\tilde{u}_k^* \triangleq \tilde{u}_k(\theta^*) = u_k - \overline{u}(\theta^*) = u_k - \Phi_k\theta^*, \tag{30}$$

$$\hat{z}_k^* \triangleq \hat{z}_k(\theta^*) = z_k - G_{\mathrm{f}}(\mathbf{q})\tilde{u}_k^*, \tag{31}$$

and

$$G_{\mathrm{c}}^*(\mathbf{q}) \triangleq G_{\mathrm{c}}(\mathbf{q},\theta^*), \tag{32}$$

$$\tilde{G}_{z\tilde{u}}^*(\mathbf{q}) \triangleq \tilde{G}_{z\tilde{u}}(\mathbf{q},\theta^*). \tag{33}$$

Since θ^* minimizes Eq. (13) for all k, for negligible R_u it follows that $\hat{z}_k^* \approx 0$, and thus

$$z_k \approx G_{\mathrm{f}}(\mathbf{q})\tilde{u}_k^*. \tag{34}$$

Hence, Eqs. (27) and (34) imply

$$\xi_k^* \triangleq \xi_k(\theta^*) \approx [G_{\mathrm{f}}(\mathbf{q}) - \tilde{G}_{z\tilde{u}}^*(\mathbf{q})]\tilde{u}_k^*. \tag{35}$$

It follows from Eq. (34) that $G_{\mathrm{f}}(\mathbf{q})$ is approximately the transfer function from $\tilde{u}_k^*$ to z_k. On the other hand, Eq. (27) with $\hat{\theta} = \theta^*$ shows that the transfer function from $\tilde{u}_k^*$ to z_k is $\tilde{G}_{z\tilde{u}}^*(\mathbf{q})$. The goal is thus to construct $G_{\mathrm{f}}(\mathbf{q})$ in order to facilitate its approximation by $\tilde{G}_{z\tilde{u}}^*(\mathbf{q})$.

To determine suitable properties of $G_{\mathrm{f}}(\mathbf{q})$, we consider the case where disturbance rejection is approximately achieved, that is, for all $k \geq 0$, $\xi_k^* \approx 0$. Under this assumption, it follows from Eq. (27) that the transfer function from $\tilde{u}_k^*$ to z_k is $\tilde{G}_{z\tilde{u}}^*(\mathbf{q})$. Now, with θ_{k+1} given by Eq. (14), it follows that Eqs. (18) and (27) become

$$\hat{z}_k(\theta_{k+1}) = z_k - G_{\mathrm{f}}(\mathbf{q})\tilde{u}_k(\theta_{k+1}), \tag{36}$$

$$z_k = \xi_k(\theta_{k+1}) + \tilde{G}_{z\tilde{u}}(\mathbf{q},\theta_{k+1})\tilde{u}_k(\theta_{k+1}). \tag{37}$$

Now assuming that $\hat{z}_k(\theta_{k+1}) \to 0$ as $k \to \infty$, Eq. (36) implies that, for all sufficiently large k,

$$z_k \approx G_{\mathrm{f}}(\mathbf{q})\tilde{u}_k(\theta_{k+1}), \tag{38}$$

and thus $G_{\mathrm{f}}(\mathbf{q})$ is approximately the transfer function from $\tilde{u}_k(\theta_{k+1})$ to z_k. Since $\tilde{G}_{z\tilde{u}}(\mathbf{q},\theta_{k+1})$ is the actual transfer function from $\tilde{u}_k(\theta_{k+1})$ to z_k, it follows that minimizing Eq. (13) drives $\tilde{G}_{z\tilde{u}}(\mathbf{q},\theta_{k+1})$ to $G_{\mathrm{f}}(\mathbf{q})$. Comparing Eq. (34) to Eq. (38) implies that

$$G_{\mathrm{f}}(\mathbf{q})\tilde{u}_k(\theta_{k+1}) \approx G_{\mathrm{f}}(\mathbf{q})\tilde{u}_k^*, \tag{39}$$

which, under sufficient persistence of excitation, implies that θ_{k+1} converges to θ^*, and thus $\tilde{G}_{z\tilde{u}}^*(\mathbf{q})$ approximates $G_{\mathrm{f}}(\mathbf{q})$. Consequently, $G_{\mathrm{f}}(\mathbf{q})$ serves as a target model for $\tilde{G}_{z\tilde{u}}^*(\mathbf{q})$.

In the case where y_k, z_k, and u_k are scalar, $\tilde{G}_{z\tilde{u}}(\mathbf{q},\theta_{k+1})$ can be written as

$$\tilde{G}_{z\tilde{u}}(\mathbf{q},\theta_{k+1}) = \frac{\mathbf{q}^{n_{\mathrm{c}}}N_{zu,\mathrm{d}}(\mathbf{q})}{D(\mathbf{q})D_{\mathrm{c}}(\mathbf{q},\theta_{k+1}) - N_{yu,\mathrm{d}}(\mathbf{q})N_{\mathrm{c}}(\mathbf{q},\theta_{k+1})}, \tag{40}$$

where $G_{zu,\mathrm{d}}(\mathbf{q}) = N_{zu,\mathrm{d}}(\mathbf{q})/D(\mathbf{q})$ and $G_{yu,\mathrm{d}}(\mathbf{q}) = N_{yu,\mathrm{d}}(\mathbf{q})/D(\mathbf{q})$. Note that the zeros of $\tilde{G}_{z\tilde{u}}(\mathbf{q},\theta_{k+1})$ include the zeros of $G_{zu,\mathrm{d}}(\mathbf{q})$. Although these zeros do not depend on $G_{\mathrm{c}}(\mathbf{q},\theta_{k+1})$, they can be canceled by roots of the denominator of $\tilde{G}_{z\tilde{u}}(\mathbf{q},\theta_{k+1})$. In the case of NMP zeros, this cancellation represents a hidden instability due to the cascade interconnection between the structure and $G_{\mathrm{c}}(\mathbf{q},\theta_{k+1})$ [28]. As shown in [15], this cancellation can be prevented by ensuring that all of the NMP zeros of $G_{zu}(\mathbf{q})$ are also zeros of $G_{\mathrm{f}}(\mathbf{q})$.

2.5. Retrospective performance variable decomposition

Substituting Eq. (37) into Eq. (36) yields

$$\hat{z}_k(\theta_{k+1}) = \xi_k(\theta_{k+1}) + [\tilde{G}_{z\tilde{u}}(\mathbf{q},\theta_{k+1}) - G_{\mathrm{f}}(\mathbf{q})]\tilde{u}_k(\theta_{k+1}). \tag{41}$$

By defining the *one-step predicted performance*

$$\hat{z}_{\mathrm{opp},k}(\theta_{k+1}) \triangleq \xi_k(\theta_{k+1}) \tag{42}$$

and the *target-model matching performance*

$$\hat{z}_{\mathrm{tmp},k}(\theta_{k+1}) \triangleq [\tilde{G}_{z\tilde{u}}(\mathbf{q},\theta_{k+1}) - G_{\mathrm{f}}(\mathbf{q})]\tilde{u}_k(\theta_{k+1}), \tag{43}$$

Eq. (41) can be written as

$$\hat{z}_k(\theta_{k+1}) \triangleq \hat{z}_{\mathrm{opp},k}(\theta_{k+1}) + \hat{z}_{\mathrm{tmp},k}(\theta_{k+1}). \tag{44}$$

The decomposition of the retrospective performance in Eq. (44) shows the interplay between the one-step predicted performance and the target-model matching performance. The one-step predicted performance represents the closed-loop response of z_k to the disturbance $w(t)$ when the controller θ_{k+1} is used, while the target-model matching performance represents the difference between $\tilde{G}_{z\tilde{u}}(\mathbf{q},\theta_{k+1})$ and $G_{\mathrm{f}}(\mathbf{q})$ driven by $\tilde{u}_k(\theta_{k+1})$. Minimizing Eq. (13) with negligible R_u yields

$$\hat{z}_k(\theta_{k+1}) \approx 0 \tag{45}$$

which, using Eq. (44) implies

$$\hat{z}_{\mathrm{opp},k}(\theta_{k+1}) + \hat{z}_{\mathrm{tmp},k}(\theta_{k+1}) \approx 0 \tag{46}$$

that is,

$$\hat{z}_{\mathrm{opp},k}(\theta_{k+1}) \approx -\hat{z}_{\mathrm{tmp},k}(\theta_{k+1}) \tag{47}$$

2.6. Standard construction of the target model

In the SISO case, note that the relative degree of $\tilde{G}_{z\tilde{u}}(\mathbf{q},\theta_{k+1})$ is equal to the relative degree of $G_{zu,\mathrm{d}}(\mathbf{q})$. Therefore, in order to facilitate model matching between $\tilde{G}_{z\tilde{u}}(\mathbf{q},\theta_{k+1})$ and $G_{\mathrm{f}}(\mathbf{q})$, we choose the relative degree of $G_{\mathrm{f}}(\mathbf{q})$ to be equal to the relative degree of $G_{zu,\mathrm{d}}(\mathbf{q})$. For the same reason, we also construct $G_{\mathrm{f}}(\mathbf{q})$ to have the same leading numerator coefficient as $G_{zu,\mathrm{d}}(\mathbf{q})$.

Furthermore, it can be seen that the numerator of $\tilde{G}_{z\tilde{u}}(\mathbf{q},\theta_{k+1})$ contains all of the zeros present in $G_{zu,\mathrm{d}}(\mathbf{q})$. Therefore, as the target-model matching performance is minimized, any NMP zeros that are present in $G_{zu,\mathrm{d}}(\mathbf{q})$, but not in $G_{\mathrm{f}}(\mathbf{q})$ can lead to unstable pole-zero cancellation. Therefore, $G_{\mathrm{f}}(\mathbf{q})$ must be constructed such that all of the NMP zeros of $G_{zu,\mathrm{d}}(\mathbf{q})$ are present in $G_{\mathrm{f}}(\mathbf{q})$.

A straightforward technique for constructing $G_{\mathrm{f}}(\mathbf{q})$ that satisfies these requirements in the SISO case is given by

$$G_{\mathrm{f}}(\mathbf{q}) = \sum_{i=0}^{n_{\mathrm{f}}} \frac{H_i}{\mathbf{q}^i}, \tag{48}$$

where H_i is the ith the Markov parameter of $G_{zu,\mathrm{d}}(\mathbf{q})$ and n_{f} is the order of $G_{\mathrm{f}}(\mathbf{q})$. In the case where the structure is minimum phase and asymptotically stable, only the first nonzero Markov parameter is used in the summation. For NMP structures, the order of n_{f} must be large enough such that the NMP zeros of $G_{\mathrm{f}}(\mathbf{q})$ approximate the NMP zeros of $G_{zu,\mathrm{d}}(\mathbf{q})$.

Note that the FIR transfer function Eq. (48) is a truncated Laurent expansion of $G_{zu,\mathrm{d}}(\mathbf{q})$ [16]. Therefore, by choosing a sufficiently large value of n_{f}, $G_{\mathrm{f}}(\mathbf{q})$ provides an approximation of $G_{zu,\mathrm{d}}(\mathbf{q})$ that is useful in the MIMO case. Unfortunately, for lightly damped structures, several hundred Markov parameters may be needed to approximate the NMP zeros; this number is prohibitively large in applications. To overcome this difficulty, we use a dereverberated transfer function as the target model.

3. Identification of dereverberated transfer functions

Let $G_{\mathrm{d}}(z)$ be a discrete-time transfer function of order n with frequency response $G_{\mathrm{d}}(\mathrm{e}^{\mathrm{j}\theta})$, where $\theta \in [0,\pi]$. The goal is to determine a dereverberated transfer function $\widehat{G}_{\mathrm{d}}(z)$ of order $\hat{n} \ll n$ whose frequency response approximates the frequency response of $G_{\mathrm{d}}(z)$. We construct $\widehat{G}_{\mathrm{d}}(z)$ by minimizing the logarithmic-average of the error between $G_{\mathrm{d}}(\mathrm{e}^{\mathrm{j}\theta})$ and $\widehat{G}_{\mathrm{d}}(\mathrm{e}^{\mathrm{j}\theta})$ subject to the constraint that all poles and zeros of $\widehat{G}_{\mathrm{d}}(z)$ are real and that $\widehat{G}_{\mathrm{d}}(z)$ is asymptotically stable. By restricting the poles and zeros to be real, we can construct a transfer function that captures the magnitude and phase trend of $G_{\mathrm{d}}(\mathrm{e}^{\mathrm{j}\theta})$ without resonances and anti-resonances. More formally, for a specified value of the maximum order $\hat{n}_{\max} \ll n$ of the dereverberated transfer function $\widehat{G}_{\mathrm{d}}(z)$, the goal is to solve the optimization problem

$$\min_{k,a,b,\hat{n},\hat{m}} \quad \int_0^{\pi} |G_{\mathrm{d}}(\mathrm{e}^{\mathrm{j}\theta}) - \widehat{G}_{\mathrm{d}}(\mathrm{e}^{\mathrm{j}\theta})|^2 \, \mathrm{d}(\log\theta) \tag{49}$$

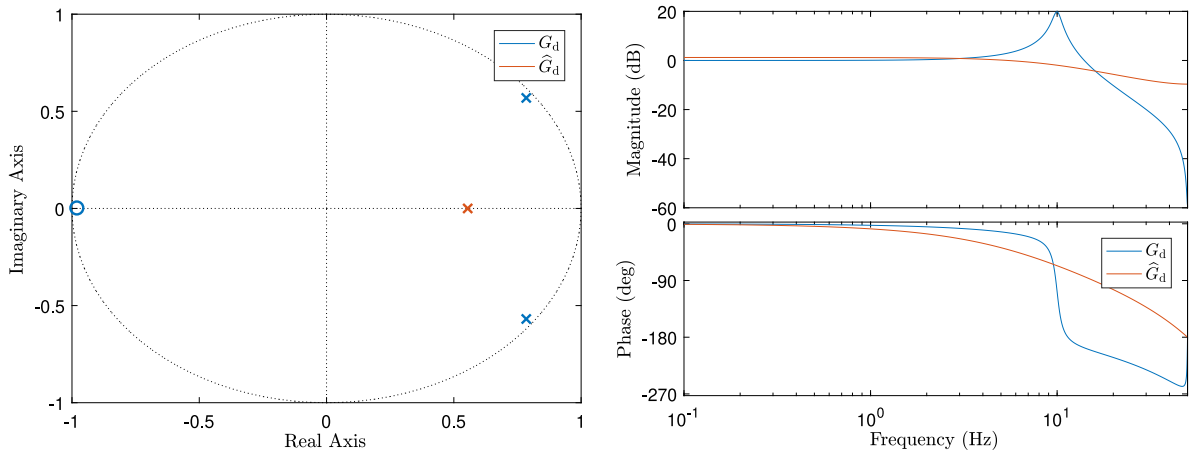

(a) (b)

Fig. 3. Dereverberated Transfer Function Example: Single-mode SISO Structure (a) Poles and zeros of the discretized structural model and the dereverberated transfer function $\hat{G}_d(z)$, which has one real pole. (b) Frequency response of $\hat{G}_d(z)$. Note that the phase of $\hat{G}_d(z)$ follows the trend of the phase of $G_d(z)$.

subject to

$$\hat{G}_d(z) = \frac{k\prod_{i=1}^{\hat{m}}(z+b_i)}{\prod_{i=1}^{\hat{n}}(z+a_i)}, \tag{50}$$

$$\hat{m} \le \hat{n} \le \hat{n}_{\max}, \tag{51}$$

$$\hat{G}_d(z) \text{ is asymptotically stable,} \tag{52}$$

where $\hat{m} \ge 0$ is the number of zeros, $a \in \mathbb{R}^{\hat{n}}$ is the vector of poles, $b \in \mathbb{R}^{\hat{m}}$ is the vector of zeros, and $k \in \mathbb{R}$ is a scaling factor. If $\hat{m} = 0$, then the numerator of $\hat{G}_d(z)$ is k. In order to simplify the optimization, $\hat{m}$ can be fixed beforehand. For example, $\hat{m}$ can be chosen such that the relative degree of the dereverberated transfer function equals the relative degree of the structure. The maximum order $\hat{n}_{\max}$ of $\hat{G}_d(z)$ is typically chosen to be much lower than the order of $G_d(z)$ in order to obtain a low-order model that efficiently captures the rolloff and phase characteristics of $G_d(z)$. For MIMO systems, the DTF is formed by solving the above optimization problem channel by channel.

3.1. Dereverberated transfer function example: Single-mode SISO structure

Consider the second-order structure with natural frequency $\omega_n = 20\pi$ rad s^{-1} and damping ratio $\zeta = 0.05$ given by

$$G(s) = \frac{(20\pi)^2}{s^2 + 2\pi s + (20\pi)^2}, \tag{53}$$

where s is the Laplace variable. Discretizing Eq. (53) with sample rate $T_s = 0.01$ s gives

$$G_d(z) = \frac{0.1871z + 0.1831}{z^2 - 1.569z + 0.9391}. \tag{54}$$

The resulting dereverberated transfer function with $\hat{n}_{\max} = 1$ is given by

$$\hat{G}_d(z) = \frac{0.5126}{z - 0.5544}. \tag{55}$$

Fig. 3 shows that the phase of $\hat{G}_d(z)$ follows the trend of the phase of $G_d(z)$ without large phase shifts. Note that for bode magnitude plots, dB is $20\log(|T(\mathrm{j}\omega)|)$ for continuous transfer functions and $20\log(|T(\mathrm{e}^{\mathrm{j}\omega T_s})|)$ for discrete transfer functions where T is the respective transfer function.

3.2. Construction of the dereverberated target model

Directly using a dereverberated transfer function for the target model G_f leads to poor disturbance rejection performance. This is due to the DTF being similar to the open loop system in magnitude. However, only a simple adjustment to the DTF is needed to improve the disturbance rejection performance. The adjusted DTF that is used as the target model G_f is termed the dereverberated target model (DTM).

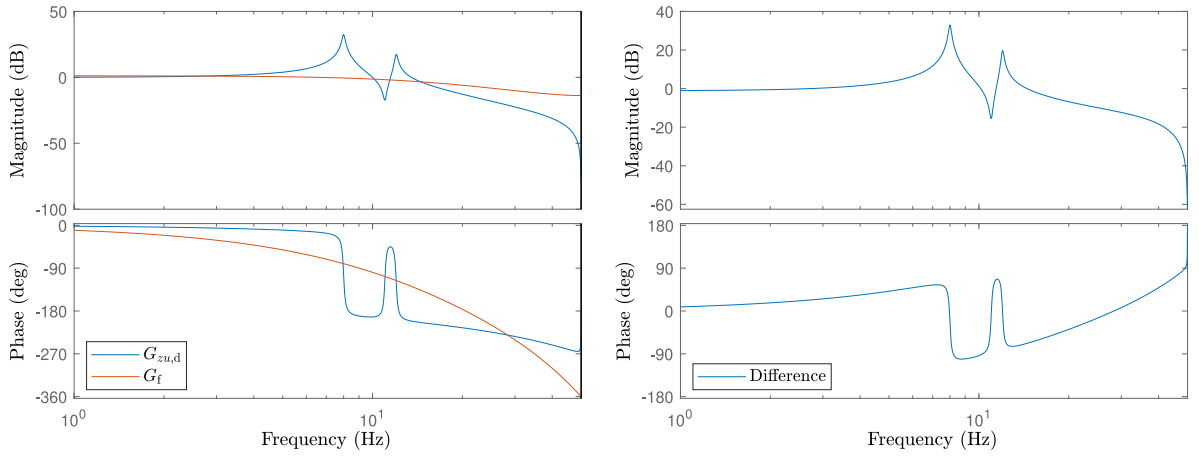

Fig. 4. Example 1: Bode plots of $G_{zu,\mathrm{d}}$ and G_{f}. The magnitude is referenced to unity gain. (a) Frequency response of the discretized G_{zu} and the DTM G_{f}. The DTM was constructed using $\hat{n}_{\max} = 2$, and $\beta = 0.8$. (b) Difference between the frequency response of the discretized G_{zu} and the DTM G_{f}.

In particular we set,

$$G_{\mathrm{f}}(z) = \beta \widehat{G}_{\mathrm{d}}(z), \tag{56}$$

where $\beta \in (0, 1]$. With $\beta \in [0.5, 0.9]$ being the values typically used. The parameter β is a tuning parameter that provides a trade off between disturbance rejection performance and robustness with smaller values of β providing better disturbance rejection performance.

4. Example 1: SISO adaptive disturbance rejection

Consider the structure given by

$$G(s) = \frac{\omega_{\mathrm{p1}}^2 \omega_{\mathrm{p2}}^2}{\omega_{\mathrm{z}}^2} \frac{s^2 + 2\zeta\omega_{\mathrm{z}} s + \omega_{\mathrm{z}}^2}{(s^2 + 2\zeta\omega_{\mathrm{p1}} s + \omega_{\mathrm{p1}}^2)(s^2 + 2\zeta\omega_{\mathrm{p2}} s + \omega_{\mathrm{p2}}^2)} \tag{57}$$

and the block diagram in Fig. 1 with $G(s) = G_{zu}(s) = G_{zw}(s) = G_{yu}(s) = G_{yw}(s)$, $T_{\mathrm{s}} = 0.01$ s, $\omega_{\mathrm{p1}} = 16\pi$ rad s^{-1}, $\omega_{\mathrm{p2}} = 24\pi$ rad s^{-1}, $\omega_{\mathrm{z}} = 20\pi$ rad s^{-1}, and $\zeta = 0.01$. The following subsections investigate the performance of RCAC for harmonic disturbance rejection using a dereverberated target model on Eq. (57) for various disturbance frequencies. Note that the frequency, amplitude, and phase of the harmonic disturbance are assumed to be unknown. As discussed in Section 2.1, all sampled-data simulations capture the intersample behavior of the structure. Measurements are corrupted by sensor noise such that there is a 60 dB SNR when measuring the asymptotic open-loop response.

The DTM is created using $\hat{n}_{\max} = 2$, and $\beta = 0.8$. The resulting dereverberated target model is shown in Fig. 4. RCAC is initialized with $n_{\mathrm{c}} = 6$, $\theta_0 = 0_{12\times 1}$, $k_w = 5n_{\mathrm{c}}$, $\lambda = 1$, $R_z = 1$, $R_\theta = 10^{-5} I_{12}$, and $R_u = 10^{-3}$. In Fig. 5, for 1000 values of the harmonic disturbance frequency ω_{d} between 4π to 50π rad s^{-1}, the ratio of the asymptotic root mean square (RMS) closed-loop and open-loop response at the sample times is plotted along with the magnitude and phase difference between $G_{zu,\mathrm{d}}(e^{\mathrm{j}\omega_{\mathrm{d}}T_{\mathrm{s}}})$ and $G_{\mathrm{f}}(e^{\mathrm{j}\omega_{\mathrm{d}}T_{\mathrm{s}}})$ and between $\tilde{G}_{z\tilde{u}}(e^{\mathrm{j}\omega_{\mathrm{d}}T_{\mathrm{s}}})$ and $G_{\mathrm{f}}(e^{\mathrm{j}\omega_{\mathrm{d}}T_{\mathrm{s}}})$. Notice that since RCAC attempts to match $\tilde{G}_{z\tilde{u}}(\mathbf{q})$ to $G_{\mathrm{f}}(\mathbf{q})$, the difference between $\tilde{G}_{z\tilde{u}}(e^{\mathrm{j}\omega_{\mathrm{d}}T_{\mathrm{s}}})$ and $G_{\mathrm{f}}(e^{\mathrm{j}\omega_{\mathrm{d}}T_{\mathrm{s}}})$ is near zero at many of the disturbance frequencies. For $\omega_{\mathrm{d}} = 16\pi$ rad s^{-1}, the closed-loop response is shown in Fig. 6. The disturbance is suppressed by 66 dB.

5. Example 2: MISO adaptive disturbance rejection

Consider the 4-mode, 2-input, 1-output structure in Fig. 7 and the block diagram in Fig. 1 with $G(s) = G_{zu}(s) = G_{zw}(s) = G_{yu}(s) = G_{yw}(s)$, and $T_{\mathrm{s}} = 0.01$ s. All poles and zeros have the same damping ratio, which is set to $\zeta = 0.1$ in Fig. 7. The following subsections investigate the performance of RCAC on a structure that has a different damping ratio than the model used to generate the dereverberated target model. Specifically, RCAC is implemented in closed-loop for 50 different values of the structural damping, ζ from 0.01 to 0.5, with a dereverberated target model computed from the nominal model with $\zeta = 0.1$. As discussed in Section 2.1, all sampled-data simulations capture the intersample behavior of the structure. Measurements are corrupted by sensor noise such that there is a 60 dB SNR when measuring the asymptotic open-loop response. There are two harmonic disturbances at $\omega_{\mathrm{d1}} = 22\pi$ and $\omega_{\mathrm{d2}} = 34\pi$ rad s^{-1} with the first input receiving the 22π rad s^{-1} disturbance and the second input receiving the 34π rad s^{-1} disturbance. Note that the frequency, amplitude, and phase of the harmonic disturbance are assumed to be unknown.

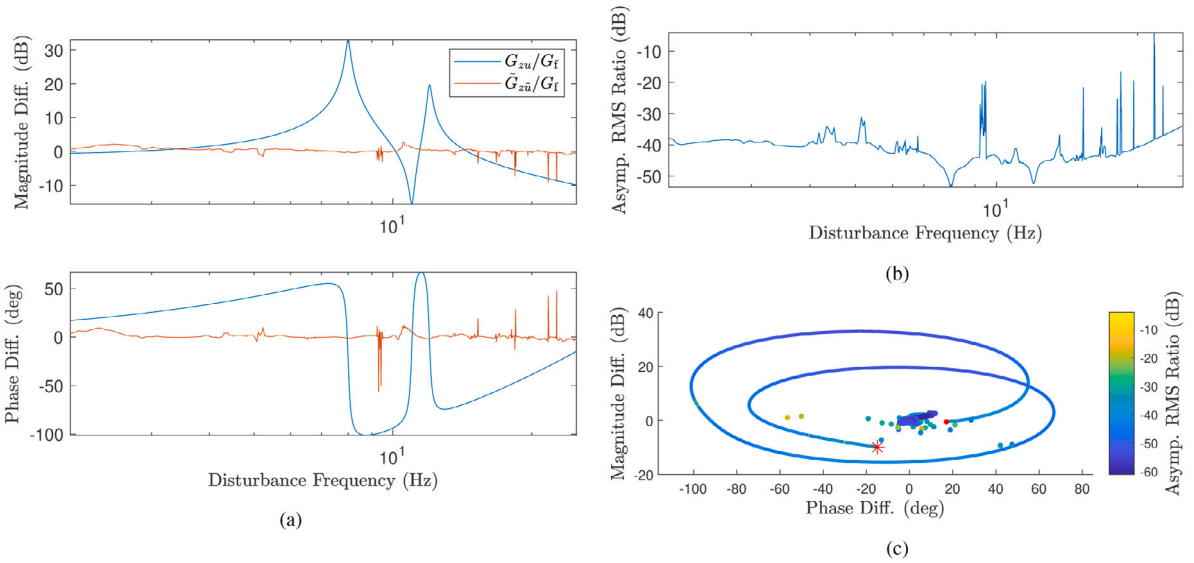

Fig. 5. Example 1: Comparison of $G_{zu,\mathrm{d}}(e^{j\omega_\mathrm{d}T_\mathrm{s}})$, $\tilde{G}_{z\tilde{u}}(e^{j\omega_\mathrm{d}T_\mathrm{s}})$, $G_\mathrm{f}(e^{j\omega_\mathrm{d}T_\mathrm{s}})$, and asymptotic RMS closed-loop response. The magnitude difference is referenced to unity gain while the asymptotic RMS ratio is referenced to the open-loop RMS response. (a) Magnitude and phase difference between $G_{zu,\mathrm{d}}(e^{j\omega_\mathrm{d}T_\mathrm{s}})$ and $G_\mathrm{f}(e^{j\omega_\mathrm{d}T_\mathrm{s}})$ and between $\tilde{G}_{z\tilde{u}}(e^{j\omega_\mathrm{d}T_\mathrm{s}})$ and $G_\mathrm{f}(e^{j\omega_\mathrm{d}T_\mathrm{s}})$ for 1000 values of the disturbance frequency between 4π to 50π rad s^{-1}. (b) Ratio of the asymptotic RMS response between closed- and open-loop versus disturbance frequency. (c) Data from Figs. 5(a) and 5(b). The points along the curve show the magnitude difference versus phase difference between $G_{zu,\mathrm{d}}(e^{j\omega_\mathrm{d}T_\mathrm{s}})$ and $G_\mathrm{f}(e^{j\omega_\mathrm{d}T_\mathrm{s}})$. The separate data points denote the magnitude difference versus phase difference between $\tilde{G}_{z\tilde{u}}(e^{j\omega_\mathrm{d}T_\mathrm{s}})$ and $G_\mathrm{f}(e^{j\omega_\mathrm{d}T_\mathrm{s}})$. On the curve, "·" corresponds to $\omega_\mathrm{d} = 4\pi$ rad s^{-1}, and "x" for $\omega_\mathrm{d} = 50\pi$ rad s^{-1}. Note that, since RCAC attempts to match $\tilde{G}_{z\tilde{u}}(\mathbf{q})$ to $G_\mathrm{f}(\mathbf{q})$, many of the separate points are near (0, 0).

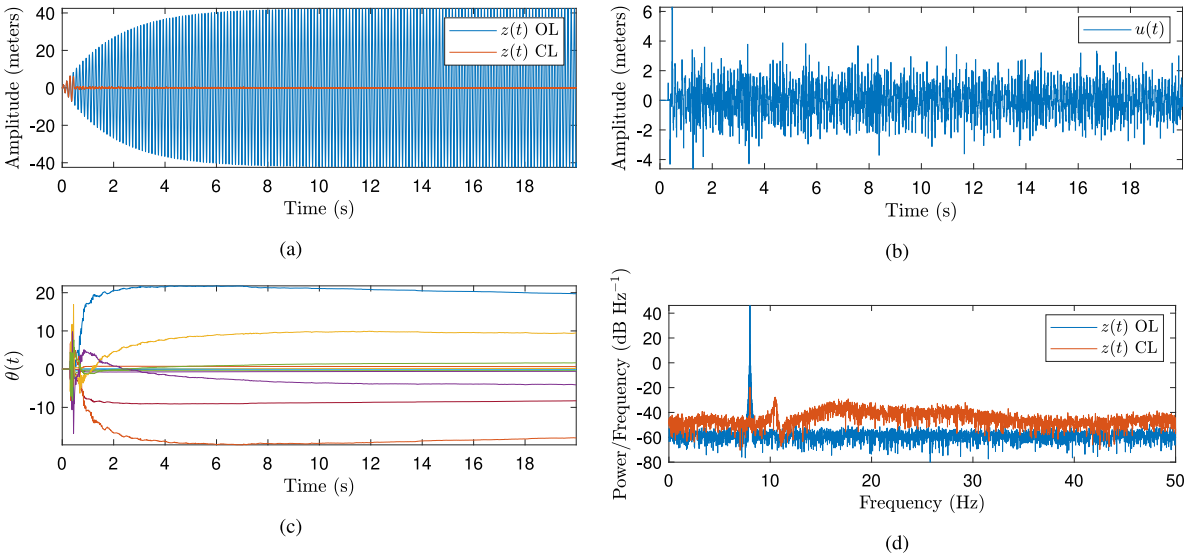

Fig. 6. Example 1: Open-loop and closed-loop response subject to the harmonic disturbance $\omega_\mathrm{d} = 16\pi$ rad s^{-1}, where RCAC starts at 0.3 s. (a) Open- and closed-loop response of z. (b) Control input. (c) Controller coefficients. (d) Power spectral density of the open- and closed-loop responses. Notice that the peak in the open-loop response corresponding to the disturbance is suppressed by 66 dB, where dB is referenced to 1 m^2.

The DTM is created using $\hat{n}_{\max} = 2$, and $\beta = 0.8$. RCAC is initialized with $n_\mathrm{c} = 8$, $\theta_0 = 0_{48\times1}$, $k_w = 5n_\mathrm{c}$, $\lambda = 1$, $R_z = 1$, $R_\theta = 10^{-6}I_{48}$, and $R_u = 10^{-2}I_2$. Fig. 8 shows the ratio of the asymptotic root mean square response between closed-loop and open-loop at the sample times along with the magnitude difference versus phase difference between $G_{zu,\mathrm{d}}(e^{j\omega_\mathrm{d}T_\mathrm{s}})$ and $G_\mathrm{f}(e^{j\omega_\mathrm{d}T_\mathrm{s}})$ and between $\tilde{G}_{z\tilde{u}}(e^{j\omega_\mathrm{d}T_\mathrm{s}})$ and $G_\mathrm{f}(e^{j\omega_\mathrm{d}T_\mathrm{s}})$ for 50 values of ζ from 0.01 to 0.5. For $\zeta = 0.01$, Fig. 9 compares the structure and the dereverberated target model constructed from the model with $\zeta = 0.1$. The resulting closed-loop response shown in Fig. 10 with the two disturbances being suppressed by 51 and 46 dB respectively.

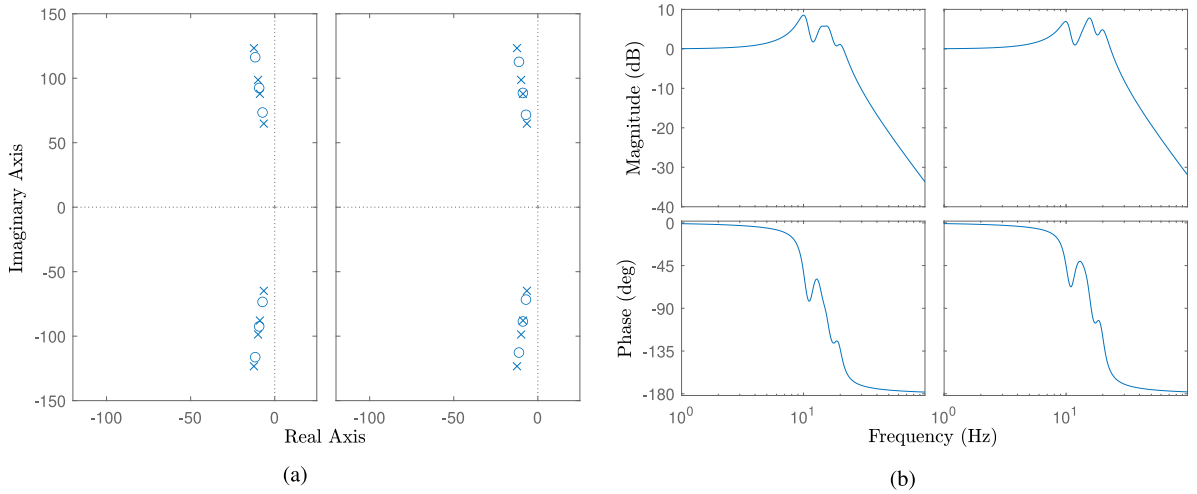

Fig. 7. Example 2: 4-mode, 2-input, 1-output structure. All poles and zeros have damping ratio $\zeta = 0.1$. Note that the left- and right-hand columns in (a) and (b) correspond to the transfer functions from u_1 and u_2, respectively, to z. (a) Pole-zero plot. (b) Frequency response. The magnitude is referenced to unity gain.

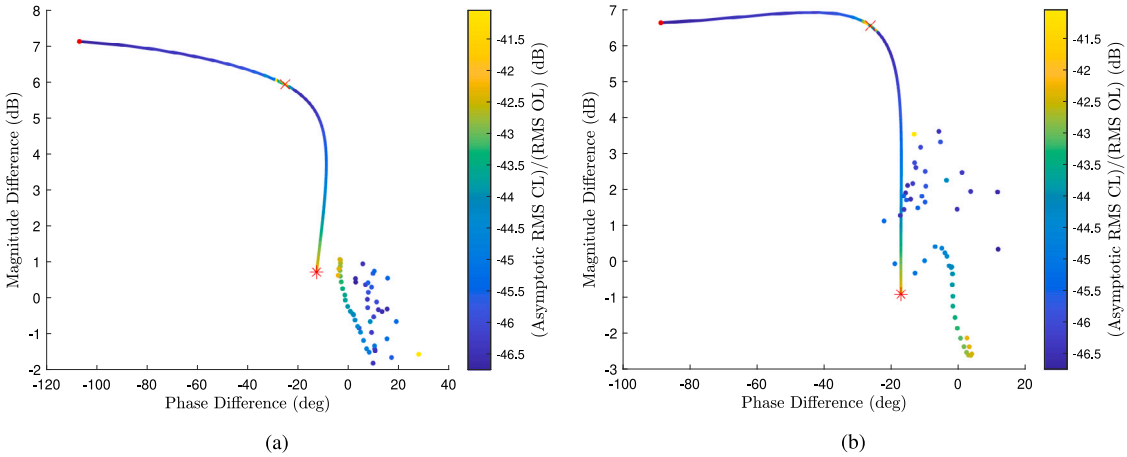

Fig. 8. Example 2: Ratio of the asymptotic RMS closed-loop response to RMS open-loop response at the sample times for 50 values of ζ between 0.01 to 0.5. The points along the curve show the magnitude difference versus phase difference between $G_{zu,\mathrm{d}}(e^{j\omega_{\mathrm{d}}T_s})$ and $G_{\mathrm{f}}(e^{j\omega_{\mathrm{d}}T_s})$. The separate data points denote the magnitude difference versus phase difference between $\tilde{G}_{z\tilde{u}}(e^{j\omega_{\mathrm{d}}T_s})$ and $G_{\mathrm{f}}(e^{j\omega_{\mathrm{d}}T_s})$. The closed-loop response uses a G_{f} computed from a model with $\zeta = 0.1$. Notice that since RCAC attempts to match $\tilde{G}_{z\tilde{u}}(\mathbf{q})$ to $G_{\mathrm{f}}(\mathbf{q})$, many of the separate points are near (0,0). The magnitude difference is referenced to unity gain while the asymptotic RMS ratio is referenced to the open-loop RMS response. On the curve, "·" corresponds to $\zeta = 0.01$, "*" for $\zeta = 0.5$, and "x" for $\zeta = 0.1$. (a) Magnitude difference versus phase difference between $G_{zu,\mathrm{d}}(e^{j\omega_{\mathrm{d}1}T_s})$ and $G_{\mathrm{f}}(e^{j\omega_{\mathrm{d}1}T_s})$ and between $\tilde{G}_{z\tilde{u}}(e^{j\omega_{\mathrm{d}1}T_s})$ and $G_{\mathrm{f}}(e^{j\omega_{\mathrm{d}1}T_s})$ for input u_1. (b) Magnitude difference versus phase difference between $G_{zu,\mathrm{d}}(e^{j\omega_{\mathrm{d}2}T_s})$ and $G_{\mathrm{f}}(e^{j\omega_{\mathrm{d}2}T_s})$ and between $\tilde{G}_{z\tilde{u}}(e^{j\omega_{\mathrm{d}2}T_s})$ and $G_{\mathrm{f}}(e^{j\omega_{\mathrm{d}2}T_s})$ for input u_2.

6. Experimental application

RCAC with a dereverberated target model is now implemented in an acoustic experiment. The experiment consists of an omnidirectional microphone with three mid-bass speakers in a 6 ft × 3 ft × 3 ft enclosed space shown in Fig. 11. One speaker w_1 is used to generate the harmonic disturbance, with the other two speakers u_1 and u_2 being available for control. The RCAC algorithm is implemented using a dSPACE SCALEXIO at a sample rate of 8 kHz. The SCALEXIO is also used to generate the harmonic disturbance consisting of seven tones at 0.8, 0.9, 1.06, 1.3, 1.6, 2.2, and 3 kHz. Note that the frequency, amplitude, and phase of the harmonic disturbance are assumed to be unknown.

The nature of the acoustic experiment leads to multi-sample delays. Once a frequency response of the system is identified, the delays are characterized and removed to facilitate the optimization procedure used to create the DTF. At 8 kHz, the delays from inputs u_1 and u_2 to the microphone corresponded to 9 and 16 samples respectively. The resulting frequency response without delays is used to generate the DTF. The 9 and 16 sample delays were then added to the appropriate inputs in the DTF to create the target model.

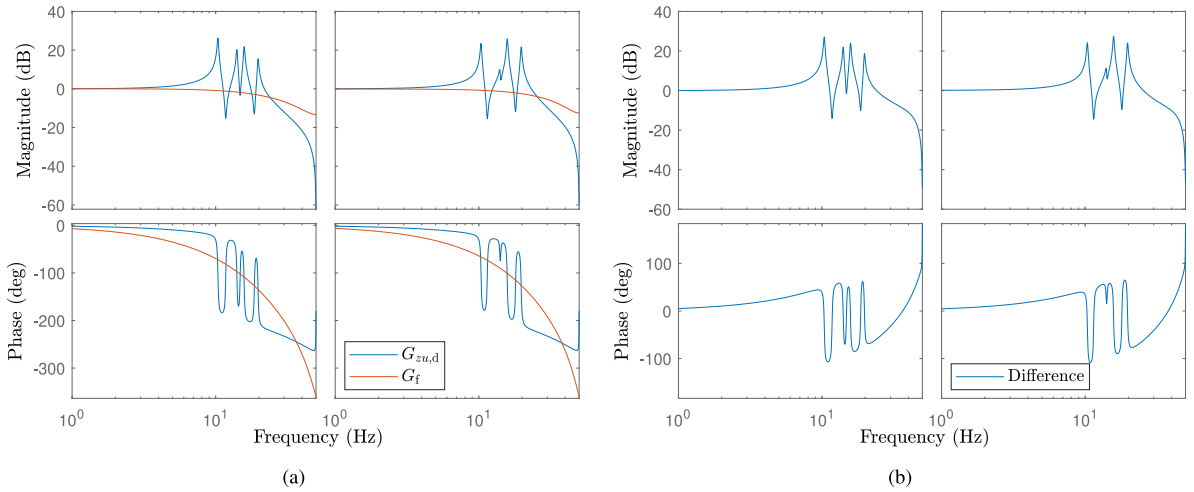

Fig. 9. Example 2: Bode plots of $G_{zu,\mathrm{d}}$ and G_{f}. Note that the left- and right-hand columns in (a) and (b) correspond to the transfer functions from u_1 and u_2, respectively, to z. The magnitude is referenced to unity gain. (a) Frequency response of the discretized G_{zu} with $\zeta = 0.01$ and the DTM G_{f} constructed from the discretized G_{zu} with $\zeta = 0.1$. The DTM was constructed by using $\hat{n}_{\max} = 2$, and $\beta = 0.8$. (b) Difference between the frequency response of the discretized G_{zu} and the DTM G_{f}.

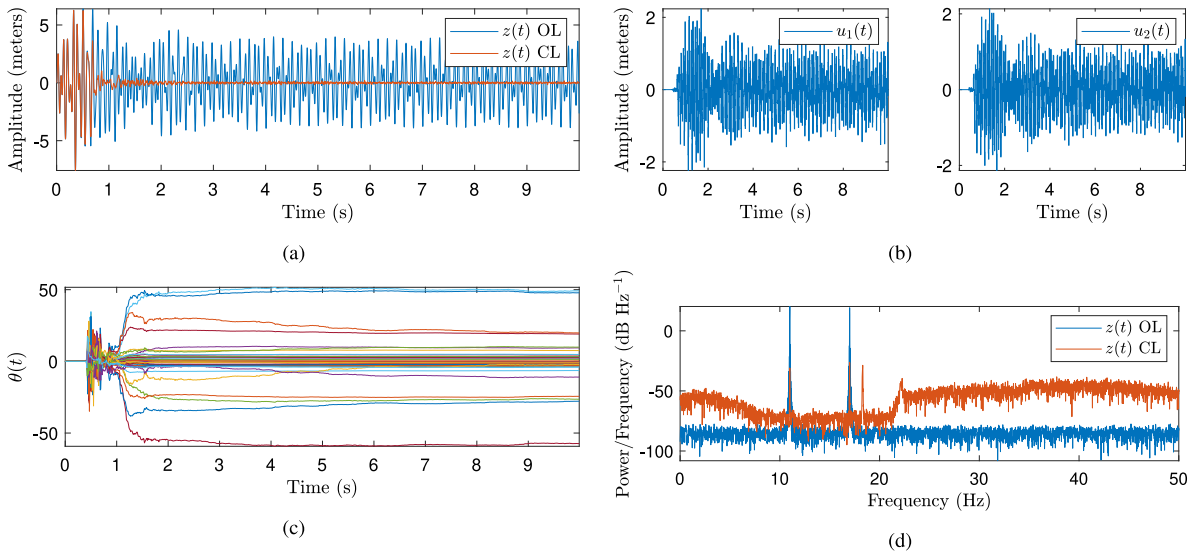

Fig. 10. Example 2: Open-loop and closed-loop response of the structure with $\zeta = 0.01$ subject to the harmonic disturbance, where RCAC starts at 0.4 s. (a) Open- and closed-loop response of z. (b) Control inputs. (c) Controller coefficients. (d) Power spectral density of the open- and closed-loop responses. Notice that the 2 peaks in the open-loop response corresponding to the disturbance are suppressed by 51 dB and 46 dB, where dB is referenced to 1 m^2.

Due to computational constraints, a modified version of RCAC was implemented for the experiment. Specifically, the controller coefficients $\hat{\theta}$ are now updated by minimizing the cost function

$$J_k(\hat{\theta}) \triangleq \frac{1}{2}(\hat{z}_k(\hat{\theta})^{\mathrm{T}}\hat{z}_k(\hat{\theta}) + \hat{\theta}^{\mathrm{T}}R\hat{\theta}), \tag{58}$$

using gradient descent, where the positive-definite matrix $R \in \mathbb{R}^{l_\theta \times l_\theta}$ is a regularization term. The update law for the controller coefficient vector is given by

$$\theta_{k+1} = \theta_k - \mu_k(\boldsymbol{\Phi}_{\mathrm{f},k}^{\mathrm{T}}\hat{z}_k(\theta_k) + R\theta_k), \tag{59}$$

where μ_k is the adaptive step size. The optimal adaptive step size can be shown to be

$$\mu_{\mathrm{opt},k} \triangleq \frac{v_k^{\mathrm{T}}(\theta_k)v_k(\theta_k)}{v_k^{\mathrm{T}}(\theta_k)(\boldsymbol{\Phi}_{\mathrm{f},k}^{\mathrm{T}}\boldsymbol{\Phi}_{\mathrm{f},k} + R)v_k(\theta_k)}, \tag{60}$$

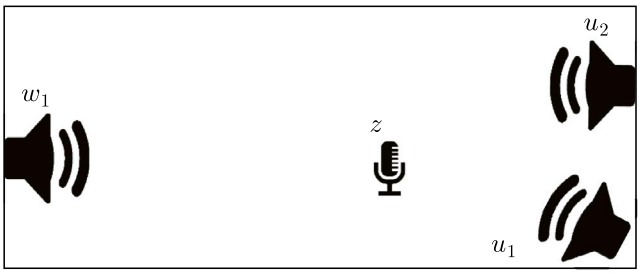

(a)

(b)

Fig. 11. Experimental Setup. (a) Simplified top-down drawing. (b) Image of experimental setup.

$$v_k(\theta_k) \triangleq (\boldsymbol{\Phi}_{\mathrm{f},k}^{\mathrm{T}}\boldsymbol{\Phi}_{\mathrm{f},k} + R)\theta_k + \boldsymbol{\Phi}_{\mathrm{f},k}^{\mathrm{T}}(z_k - u_{\mathrm{f},k}). \tag{61}$$

For computational convenience, the step size is chosen to be

$$\mu_k = \frac{\alpha}{\|\boldsymbol{\Phi}_{\mathrm{f},k}\|_{\mathrm{F}}^2} \leq \mu_{\mathrm{opt},k}, \tag{62}$$

where $\|\cdot\|_{\mathrm{F}}$ is the Frobenius norm and $\alpha > 0$ is chosen to adjust the speed of the adaptation.

The DTM is created using $\hat{n}_{\max} = 6$, and $\beta = 0.6$. RCAC is initialized with $n_{\mathrm{c}} = 40$, $\theta_0 = 0_{240\times1}$, $k_w = 14n_{\mathrm{c}}$, $\alpha = 0.05$, and $R = 0$. Fig. 12 compares the acoustic experiment model and the dereverberated target model. Fig. 13 shows that the disturbance is suppressed as the controller coefficients converge.

7. Conclusions and future research

In this paper, dereverberated transfer functions were constructed from frequency-domain data by averaging both magnitude and phase data. For harmonic disturbance rejection in a sampled-data feedback loop, retrospective cost adaptive control was applied numerically to adaptive disturbance rejection using a dereverberated transfer function as the target model. The frequency, amplitude, and phase of the harmonic disturbance were assumed to be unknown. Using the limited modeling information provided by the low-order dereverberated target model, RCAC was found to suppress the harmonic disturbance over a range of disturbance frequencies. In addition, for a 2-input, 1-output structure, RCAC was found to suppress the harmonic disturbance using a dereverberated target model constructed from a model with an erroneous damping ratio.

RCAC was then applied to a 2-input, 1-output acoustic noise-suppression experiment. A gradient-based variation of RCAC was implemented with a dereverberated target model with 8 kHz sample rate, with seven harmonic disturbances. RCAC was found to suppress the disturbances as well as ambient disturbances present in the lab. The results show that a dereverberated target that captures the phase and magnitude trend but not the detailed peaks and notches of the structure can be effective for lightly damped structures.

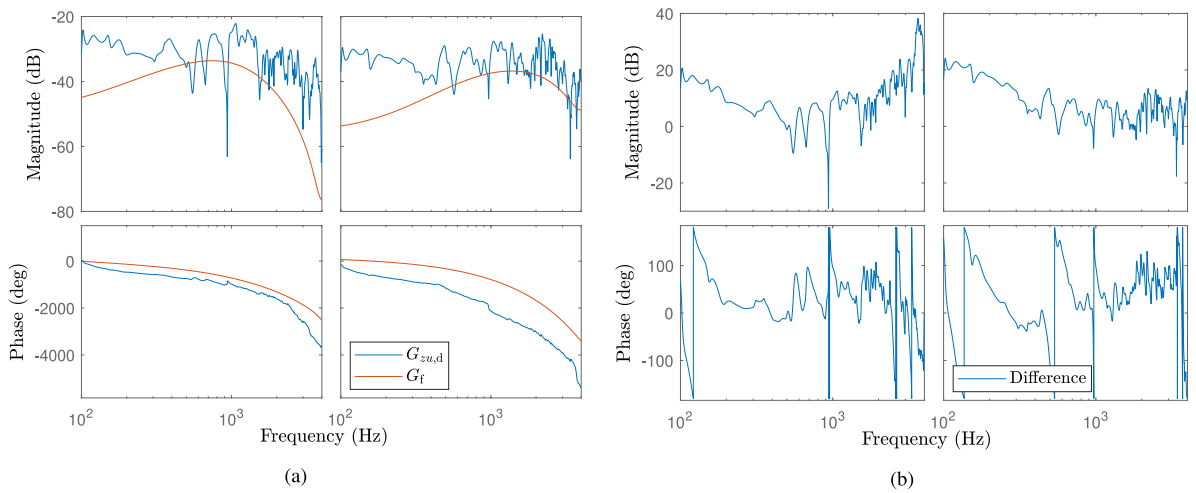

Fig. 12. Experiment: Bode plots of $G_{zu,\mathrm{d}}$ and G_{f}. Note that the left- and right-hand columns in (a) and (b) correspond to the transfer functions from u_1 and u_2, respectively, to z. The magnitude is referenced to unity gain. (a) Frequency response of the discretized G_{zu} and the DTM G_{f}. The DTM was constructed using $\hat{n}_{\max} = 6$, $\beta = 0.6$, and adding a 9 sample delay to input u_1 and 16 sample delay to input u_2. (b) Difference between the frequency response of the discretized G_{zu} and the DTM G_{f}.

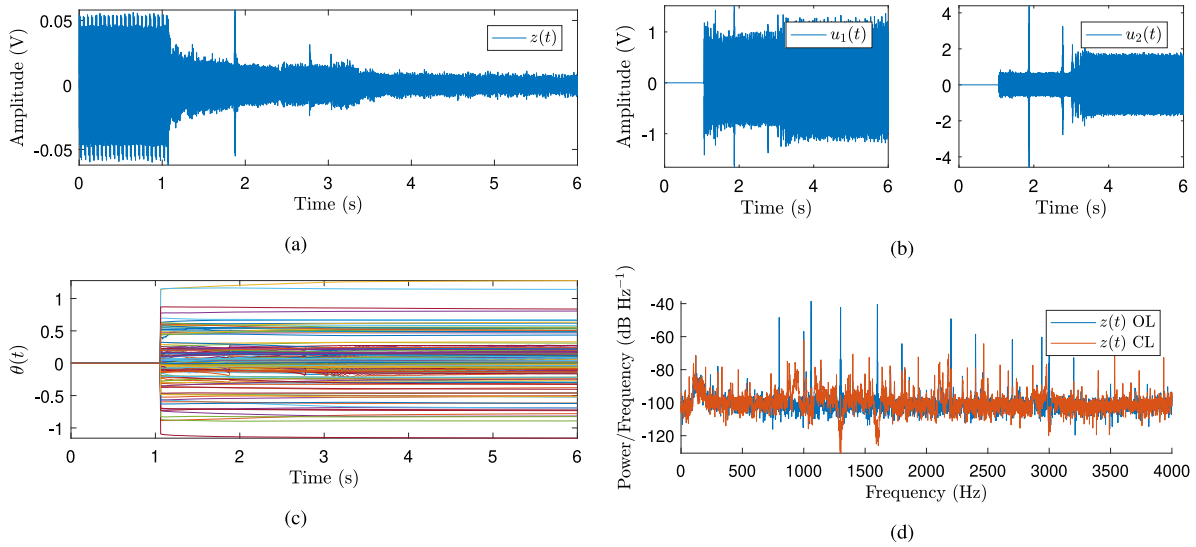

Fig. 13. Experiment: Open-loop and closed-loop response of the acoustic experiment subject to the harmonic disturbance, where RCAC starts at 1.05 s. (a) Closed-loop response of z. (b) Control inputs. (c) Controller coefficients. (d) Power spectral density of the open- and closed-loop responses, where dB is referenced to 1 V^2. Notice that the 7 largest peaks in the open-loop response corresponding to the disturbance are suppressed in the closed-loop response to the noise floor. Disturbances from the laboratory environment are also present.

CRediT authorship contribution statement

Nima Mohseni: Conceptualization, Software, Investigation, Writing – original draft, Visualization. **Dennis S. Bernstein:** Supervision, Resources, Writing – review & editing.

Declaration of competing interest

The authors declare that they have no known competing financial interests or personal relationships that could have appeared to influence the work reported in this paper.

Acknowledgments

This work was supported by a NASA Space Technology Graduate Research Opportunity [grant number 80NSSC20K1164].

References

[1] C.R. Fuller, A.H. von Flotow, Active control of sound and vibration, IEEE Control Syst. Mag. 15 (1995) 9–19, http://dx.doi.org/10.1109/37.476383.
[2] P.A. Nelson, S.J. Elliot, Active Control of Sound, Academic Press, 1992, http://dx.doi.org/10.1049/ecej:19900032.
[3] S.M. Kuo, D.R. Morgan, Active Noise Control Systems: Algorithms and DSP Implementations, Wiley, 1995.
[4] A. Preumont, Vibration Control of Active Structures: An Introduction, fourth ed., Springer, 2018, http://dx.doi.org/10.1007/978-3-319-72296-2.
[5] D. Abramovitch, G. Franklin, A brief history of disk drive control, IEEE Control Syst. Mag. 22 (2002) 28–42.
[6] R.J. Benhabib, R.P. Iwens, R.L. Jackson, Stability of large space structure control systems using positivity concepts, J. Guid. Control 4 (1981) 487–494, http://dx.doi.org/10.2514/3.56100.
[7] M.D. McLaren, G.L. Slater, Robust multivariable control of large space structures using positivity, J. Guid. Control Dyn. 10 (1987) 393–400, http://dx.doi.org/10.2514/3.20230.
[8] S.M.S.M. Joshi, Control of Large Flexible Space Structures, Springer-Verlag, Berlin, 1989.
[9] R. Lozano-Leal, S.M. Joshi, On the design of the dissipative LQG-type controllers, in: Proceedings of the 27th IEEE Conference on Decision and Control, vol. 2, 1988, pp. 1645–1646, http://dx.doi.org/10.1109/CDC.1988.194606.
[10] J.R. Forbes, C.J. Damaren, Single-link flexible manipulator control accommodating passivity violations: Theory and experiments, IEEE Trans. Control Syst. Technol. 20 (2012) 652–662, http://dx.doi.org/10.1109/TCST.2011.2122307.
[11] M.M. Seron, J.H. Braslavsky, G.C. Goodwin, Fundamental Limitations in Filtering and Control, Springer, New York, 1997.
[12] B. Widrow, S.D. Stearns, Adaptive Signal Processing, volume 15, Prentice Hall Englewood Cliffs, NJ, 1985.
[13] S.M. Kuo, D.R. Morgan, Active noise control: A tutorial review, Proc. IEEE 87 (1999) 943–973, http://dx.doi.org/10.1109/5.763310.
[14] R.L. Clark, W.R. Saunders, G.P. Gibbs, Adaptive Structures: Dynamics and Control, Wiley, 2001.
[15] Y. Rahman, A. Xie, D.S. Bernstein, Retrospective cost adaptive control: Pole placement, frequency response, and connections with LQG control, IEEE Control Syst. Mag. 37 (2017) 85–121.
[16] S. Dai, Z. Ren, D.S. Bernstein, Adaptive control of nonminimum-phase systems using shifted Laurent series, Internat. J. Control 90 (2017) 409–422.
[17] J.B. Hoagg, M.A. Santillo, D.S. Bernstein, Discrete-time adaptive command following and disturbance rejection with unknown exogenous dynamics, IEEE Trans. Automat. Control 53 (2008) 912–928, http://dx.doi.org/10.1109/TAC.2008.920234.
[18] J.B. Hoagg, D.S. Bernstein, Retrospective cost model reference adaptive control for nonminimum-phase systems, AIAA J. Guid. Control Dyn. 35 (2012) 1767–1786, http://dx.doi.org/10.2514/1.57001.
[19] D.G. MacMartin, S.R. Hall, Broadband control of flexible structures using statistical energy analysis concepts, J. Guid. Control Dyn. 17 (1994) 361–369.
[20] E. Skudrzyk, The mean-value method of predicting the dynamic response of complex vibrators, J. Acoust. Soc. Am. 67 (1980) 1105–1135, http://dx.doi.org/10.1121/1.384169.
[21] A.S. Purekar, D.J. Pines, Detecting damage in non-uniform beams using the dereverberated transfer function response, Smart Mater. Struct. 9 (2000) 429–444.
[22] J. Ma, D.J. Pines, Concept of dereverbation and its application to damage detection in civil structures, in: Proceedings SPIE, vol. 3988, 2000, pp. 127–134, http://dx.doi.org/10.1117/12.383133.
[23] K. Matsuda, H.A. Fujii, Analysis of the dereverberated transfer function in finite dimensions, J. Guid. Control Dyn. 19 (1996) 91–98.
[24] D.G. Mac Martin, S.R. Hall, Control of uncertain structures using an H(infinity) power flow approach, J. Guid. Control Dyn. 14 (1991) 521–530, http://dx.doi.org/10.2514/3.20671.
[25] C.H. Hodges, J. Woodhouse, Theories of noise and vibration transmission in complex structures, Rep. Progr. Phys. 49 (1986) 107–170.
[26] M.D. Sidman, F.E. Verghese, D. G.C., Parametric system identification on logarithmic frequency response data, IEEE Trans. Automat. Control 36 (1991) 1065–1070.
[27] S.A.U. Islam, D.S. Bernstein, Recursive least squares for real-time implementation, IEEE Control Syst. Mag. 39 (2019) 82–85, http://dx.doi.org/10.1109/MCS.2019.2900788.
[28] J.B. Hoagg, D.S. Bernstein, Nonminimum-phase zeros: Much to do about nothing, IEEE Control Syst. Mag. 27 (2007) 45–57.